Synergy of the ray tracing+carrier transport approach: on efficiency of perovskite solar cells with a back reflector

Francesc Bonnín-Ripoll[1], Yaroslav B. Martynov[2], Gabriel Cardona[3] , Rashid G. Nazmitdinov[4,5] and Ramon Pujol-Nadal[1].

[1] *Departament de Física, Universitat de les Illes Balears, E-07122 Palma de Mallorca, Spain.*

[2] *State Scientific-Production Enterprise "Istok" 141120 Fryazino, Russia.*

[3] *Departament de Matemàtiques, Universitat de les Illes Balears, E-07122 Palma de Mallorca, Spain.*

[4] *Bogoliubov Laboratory of Theoretical Physics, Joint Institute for Nuclear Research, 141980 Dubna, Russia.*

[5] *Dubna State University, 141982 Dubna, Moscow region, Russia.*

Abstract

We investigate the absorptance and the power conversion efficiency of a perovskite thin-film solar cell at a specular and Lambertian reflection on the cell's back-surface reflector. The analysis is done by means of the Monte-Carlo ray tracing simulations, complemented by the transfer-matrix method to account for the interference phenomenon in the local generation rate $G(z)$ of carriers inside the semiconductor. This function is employed further in the transport equations to calculate the current-voltage characteristics of the cell. Taking the perovskite absorber $CH_3NH_3PbI_3$ as an example, we analyse its efficiency, altering the absorber thickness in the interval $50 \div 1000$ nm. We find that in the cell (~ 200 nm) the enhanced photon absorption due to the Lambertian reflection yields the efficiency increase on 2.2% as opposed to the specular reflection case. Moreover, the maximum efficiency, obtained for the perovskite layer of the thickness ~ 150 nm, exceeds the one obtained for the perovskite layer of the thickness ~ 500 nm with the specular reflection.

Keywords: solar cell, perovskite, thin-film, ray tracing, TMM, the Lambertian scattering, electron/hole current, power conversion efficiency.

1. Introduction

Novel materials and thin-film assemblies have been proposed recently for new designs of thin-film solar cells (1; 2). One of the basic requirements to photovoltaics elements is to operate with active absorbing layer width of the order of a micron or even less to produce flexible films for various applications. Therefore, organic-inorganic perovskite (having good physico-chemical properties: direct band gap, high carrier mobility, and large carrier diffusion lengths) attract a tremendous attention due to their low-cost and potential for high efficiency. Indeed, during a few last years perovskite solar cells (PSCs) demonstrate a remarkable improvement the power conversion efficiency (PCE), reaching nowadays the figure 23.7% (3). Submicron films made from such a semiconductor can absorb most incident sunlight, in contrast to the hundreds of micrometers, typically found in crystalline Si solar cells. It is noteworthy to mention that the decrease of thickness would allow to involve as well hot electrons in further efficiency increase. The natural question arises: is there any restriction on the thickness of the perovskite absorber? Another related question: does exist an optimal thickness that could yield the maximal efficiency for the perovskite solar cell with a chosen absorber?

Evidently, the availability of an effective absorber is a necessary but still an insufficient condition to construct the *efficient* thin-film perovskite solar cell (PSC). There are different elements that create such a thin-film multi-layer structure. The interplay of various layers properties determine finally the PCE of a realistic solar cell. Therefore, there is a strategic imperative to develope a general approach starting from the basic semiconductor physics, complemented by various known and less known physical mechanisms that may affect the energy conversion (see below). Evidently, by means of the numerical simulations within such the approach one can analyze the optical efficiency under different working conditions, such as: radiation, temperature, incidence angle, solar aureole, novel materials, etc. The methodology, based on such numerical simulations, is cheaper and flexible. It allows to analyze the novel architecture of a solar cell during the design period, or even to optimize it before manufacture. The major goal of the present paper is to suggest such the approach. Its vitality will be validated, comparing the simulated results with available experimental data for a typical thin-film

solar cell with the perovskite absorber $CH_3NH_3PbI_3$.

Photovoltaic cell can be defined as an opto-electronic device whose function is to absorb the maximum of the solar radiation and convert it into the electricity with a maximal efficiency. It is possible to optimize highly the energy conversion before building any physical prototype. There are a few important ingredients in a real solar cell that should operate efficiently as well as the effective absorber. Among them is the optics, capturing solar radiation and utilizing it via photovoltaics. It is the key underpinning for improving solar energy conversion technologies. Indeed, if the solar systems present light trapping mechanisms, optics is of utmost important during the initial stages of development of a new prototype. Often these devices present complex geometries, such as concentrating lenses or pyramidal textures, in order to maximize the PCE. One of the most common tools used to determine the optics of complex solar systems with a high accuracy is the so called Monte-Carlo ray tracing simulation. It consists of a set of techniques that determine the path of light through matter in a three-dimensional (3D) environment with computer simulations (4). It helps to analyze the performance of solar cells, due to the ability to perform optical simulations of systems with complex geometries [e.g., (5), (6), (7), (8)]. We implement in our approach the Monte-Carlo ray tracing technique, adding the transfer-matrix method (TMM) to characterize the optical response of the PSC. Note, that in all these studies, mentioned above, J–V characteristics, that define objectively the system efficiency, are missing. Evidently, it is quite desirable to provide "a bridge" that could relate the ray tracing results with the PCE of a solar cell, that depends on a number of generated electron-hole pairs.

The next step of the efficiency improvement of thin solar cells may be achieved by light trapping mechanisms [e.g., (9),(10),(11),(12)]. It is important to mention that rigorous optical models, that consider all the effects regarding the radiation-matter interaction mentioned above, are needed to elucidate the number of absorbed photons inside the active materials. In the standard approaches (13) the rate G of creation of pairs of electrons/holes is considered with a few serious simplifications: i) only photons that impact on the upper surface of the solar cell are included; ii) the normal incidence of light is taking into account only; iii) reflections on the backside of the solar cell are neglected; iv) the interference effects in thin films are missing; v) the light trapping mechanism are not included.

We remove these restrictions, that are too unrealistic, and analyze the consequences. In our approach this rate is a position-dependent function

(see below). According to a general wisdom, the net of generated electron-hole pairs depends substantially on generation and recombination rates of carriers. If the pair is generated away from the contact, it has a greater chance of being recombined. Evidently, at the conversion of light to electricity, we may increase either the thickness of a PSC (it is not desirable) or to decrease the recombination rates. We will trace how the thickness and an arbitrary incidence of light may affect the recombination. In addition, combining with some light trapping mechanism, we will investigate how the both mechanisms might increase the generation, and, therefore, the electrical gain of a thin-film solar cell. To this aim, we consider the most simple trapping mechanism, related to properties of a back-surface reflector (BSR). If the wavelength of the incoming light is of the order of magnitude of the film thickness, the interference phenomenon becomes important. In this regard, the integration of ray tracing simulations, taking into account the coherence phenomenon by means of the TMM, into the resolution of carrier-transport equations for solar cells, should provide quite reliable prediction on the J–V characteristics.

To the best of our knowledge, there are not available models that allow to determine with a high accuracy the generation ratio locally. Therefore, it is expected that an approach, that couples the optics equations with the carrier transport equations, will provide the objective certainty of the efficiency of the solar cell samples/models. Another goal of our approach is to elucidate the role of the BSR on the J–V characteristics, and, consequently, on the PCE of the solar cell. To reach the latter aim we consider two models of the BSR: a specular reflection model and a total diffuse reflection model with the Lambertian scattering. Finally, we will present the results for the PCE of the cell with different BSRs, and for various perovskite layer thickness in the range $50 \div 1000$ nm.

Thus, we would like to present the advanced approach that enables to one to design a solar cell with certain requirements to attain a maximum efficiency for a chosen cell's architecture. In fact, we will propose the model, taking into account highly relevant optical effects that are not generally contemplated in the literature. Therefore, we are expecting that the application of the novel concepts for PSCs, discussed in our paper, will provide a useful impetus for new technological developments.

2. Basic elements of the model calculations

2.1. Optical model

To analyze the dependence of optical properties on the BSR, we use ray tracing simulations with the aid of the ray trace OTSun python package (14). This software allows to perform the simulations by loading a geometry file designed with the aid of FreeCAD (15), an open source software for the parametric modeling of geometric figures in 3D. Note, that any geometry configuration can be drawned using FreeCAD in order to perform a ray tracing simulation. Furthermore, OTSun has the web application (16; 17) to carry out simulations in a simpler and faster way.

OTSun considers Fresnel equations and light polarization to determine the trajectory and the energy of each ray in a solar optical system. The Fresnel coefficients describe the amplitudes of the reflected, R, and transmitted, T, waves at an interface for both parallel and perpendicular components (18):

$$R = \left(\frac{\eta_1 - \eta_2}{\eta_1 + \eta_2}\right)\left(\frac{\eta_1 - \eta_2}{\eta_1 + \eta_2}\right)^* , \tag{1}$$

$$T = \frac{4\eta_1 Re(\eta_2)}{(\eta_1 + \eta_2)(\eta_1 + \eta_2)^*} . \tag{2}$$

In Eqs.(1,2) the optical admittance of the material η_i $(i = 1, 2)$ depends on the polarization of the incident light, as shown below:

$$\eta_i = \begin{cases} \tilde{n}_i(\lambda)\cos\theta_i / Z_0 & \text{for s-polarization}\,, \\ \tilde{n}_i(\lambda)/[\cos\theta_i Z_0] & \text{for p-polarization}\,. \end{cases} \tag{3}$$

Here, $Z_0 = \sqrt{\mu_0/\epsilon_0}$ is the optical impedance of a free space; θ_i is the incidence angle; $\tilde{n}_i(\lambda) = n_i(\lambda) - ik_i(\lambda)$ is the complex refractive index; and λ is the light wavelength.

According to the Lambert-Beers law for a given absorption coefficient $\alpha(\lambda) = 4\pi k(\lambda)/\lambda$ of a material, the number of absorbed photons is a function of the path length ℓ:

$$N(\ell, \lambda) = N_0(0, \lambda) e^{-\alpha(\lambda)\ell} . \tag{4}$$

Here, $N_0(0, \lambda)$ is the initial number of photons of the incident ray on a material (for each time when a ray impacts onto a material according to the

path trajectories determined by the ray tracing simulation); ℓ is the path length of the light beam through a material. With the aid of OTSun (that simulates the path trajectories) and Eq.(4), we calculate the generation rate locally in the considered semiconductor by means of the following equation

$$G(z) = \sum_{\lambda} \frac{\Delta N}{\Delta V}\,, \tag{5}$$

where ΔN is the amount of absorbed photons in the volume ΔV, $z = \ell \cos\theta$ is the depth from a semiconductor surface, and θ is the ray refracted angle. In the limit $\Delta V \to 0$, Eq.(5) transforms to the expression:

$$G(z) = \int_0^{\infty} \alpha(\lambda) N_0(0,\lambda) e^{-\alpha(\lambda) z/\cos\theta} d\lambda\,. \tag{6}$$

The thin-film multilayer structure (analyzed in our paper, see Fig.1) consists of a typical set of materials used for high-efficiency device performance [e.g.,(9; 19; 20)]. The top of the system is composed of the BK7 glass cover coated with the MgF_2 antireflecting film, followed by an indium tin oxide (ITO) layer as a transparent conducting oxide. A compact layer of TiO_2, acting as the electron transport material (ETM), is deposited over the most widely studied perovskite absorber, $CH_3NH_3PbI_3$. Finally, there are the hole-transporter material (HTM), Spiro-OMeTAD layer, and the silver back contact, connected to the external circuit. The widths of the MgF_2 and the TiO_2 have been calculated according to the antireflection coating condition at the wavelength $\lambda = 550$nm (18). We recall that our major goal is to understand the basic mechanisms that may affect the PCE of the perovskite absorber at fixed values of physical parameters of other layers. Therefore, we use for these layers the parameters that are taken from experimental data. In particular, Kaminski et al. have found an optimized value of 62nm for the ITO thickness (21). The typical thickness of the Spiro-OMeTAD layer varies from 100 to 500 nm (22; 23). Based on the results Refs. (9; 24), we fix the value 250 nm for the Spiro-OMeTAD layer thickness. The optical properties of the considered materials (the refractive index n and the extinction coefficient k as a function of wavelength) are taken from experimental data (25; 26; 27; 28; 29; 30; 31).

Fig.1 displays the schematic picture of the optical model, that describes the antireflection coating and the reflection on the BSR. The specular reflection is based on the reflection law, applicable to smooth surfaces. In turn, the

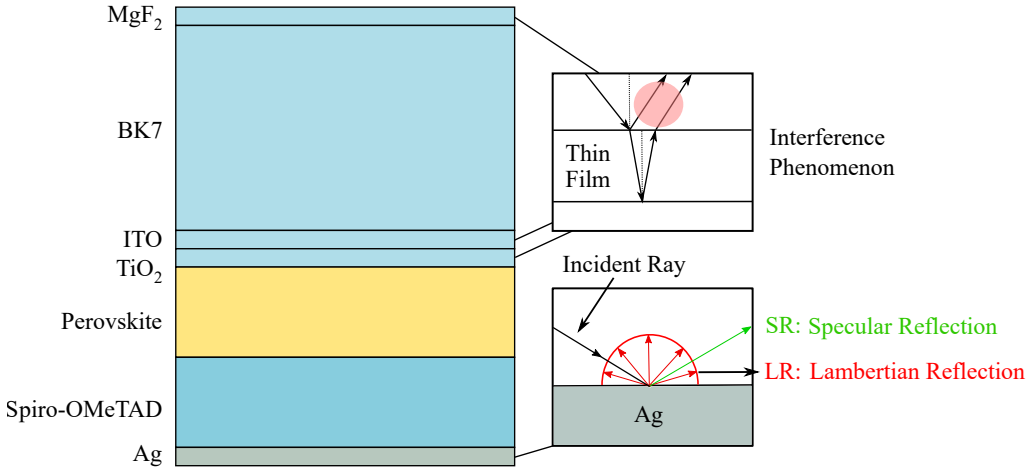

Figure 1: Left: Sketch of the thin-film system. It composed of: MgF_2 (99.8 nm) (32) / BK7 glass (1 mm) (30) / ITO (62 nm) (29) / TiO_2 (56.5 nm) (27) / Pervoskite ($200 \div 1000$ nm) (25) / Spiro-OMeTAD (250 nm) (28) / Ag (31). Here, z is the depth from a semiconductor surface. Right: Sketch of optical phenomena that take place on the antireflecting coating and on a BSR.

Lambertian case is based on a total diffuse reflection due to a microscopically random surface structure. It exerts influence upon the direction of reflected rays and disperses the energy flux spatially. To preserve the coherence transmittance between layers, the TMM algorithm is used to calculate the optical polarization response by using the python package (33).

We recall that it consists in the determination of polarized: (i) reflectance, (ii) transmittance, and (iii) material absorptance. We neglect the coherence for the glass due to its thickness.

2.2. Validation of the optical model

The OTSun python package allows to simulate the effect of interference phenomenon in thin-films in a solar optical system, using the polarized reflection, transmittion and absorption coefficients, calculated externally. The coefficients of the set of layers above the perovskite layer are calculated with the aid of the TMM algorithm (33). Note, that in the OTSun simulations the properties of this set have been associated with those of an effective single layer. In presently available the OTSun package the interference phenomenon inside the semiconductor is omitted. Consequently, the perovskite and Spiro-OMeTAD layers should be considered as incoherent in the simula-

tions. In the both materials interference effects are, however, expected, since their thicknesses are similar to the wavelength of the incoming light.

In order to quantify this discrepancy in the most sensitive case, i.e., in the specular BSR one, we apply the TMM algorithm. It is used to determine the absorptance in the perovskite layer at the condition of presence and absence of the coherence for the perovskite and the Spiro-OMeTAD layers. The analysis is done at the normal incident direction of light. The results demonstrate a close correspondence between incoherent and coherent cases for the perovskite thickness 200 nm (see Fig.2a). The difference between the number of photons, absorbed in the two situations, is less than 2% considering the standard AM1.5 ASTM G-173-03 reference direct spectrum (34). Note that the discrepancy decreases with the increase of the layer thickness. On the other hand, if the thickness is less than 200 nm, the discrepancy is high enough to not consider these thicknesses in the specular case. These results imply that if the Lambertian reflection model is considered for the Ag layer, due to the ray random distribution, the interference inside the both layers are not likely expected. Thus, our results imply that the perovskite and the Spiro-OMeTAD layers can be considered as incoherent.

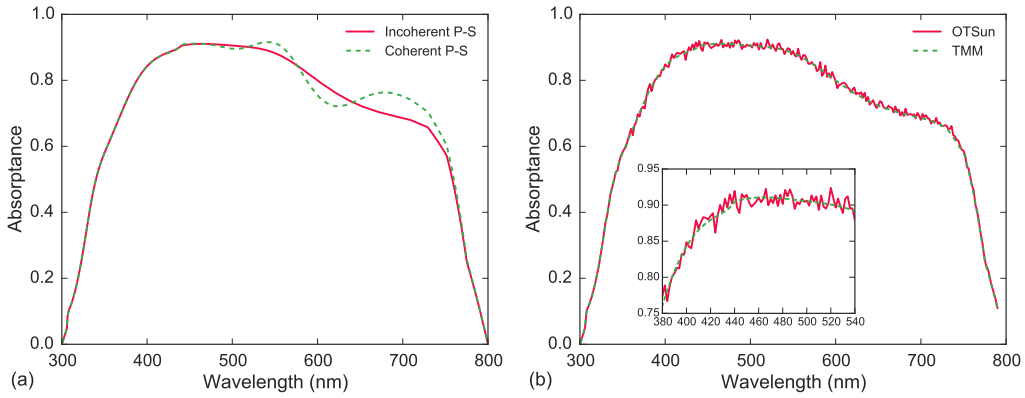

Figure 2: (a) The absorptance of the perovskite layer calculated with the TMM algorithm for both coherent and incoherent perovskite and Spiro-OMeTAD. (b) Absorptance of the perovskite layer in the incoherent case, calculated with TMM and OTSun ray trace.

Next, we proceed to validate the analysis, based on the OTSun simulations. To this aim we compare the results at normal incidence for the absorptance in the perovskite layer, obtained with the aid of OTSun ray trace and with the TMM algorithm for the specular BSR (see Fig.2b). In

total, 1000 rays are emitted per each wavelength with a 2 nm step in the ray trace simulation. The results demonstrate a remarkable agreement between two approaches. This fact, indeed, confirms, the vitality of the optical method, based on the OTSun simulations.

2.3. Carrier transport

To calculate J–V characteristics of an illuminated solar cell with different BSRs, we employ the model (35). It allows to incorporate generation rates for carrier transfers into the continuity equations for electrons in a conduction band and for holes in a valence band. For the sake of discussion let us recapitulate the basic elements of this model.

We consider the following set of equations for electron/hole density $\eta = n/p$:

$$\frac{\partial \eta}{\partial t} + \frac{1}{q}\vec{\nabla} \cdot \vec{j}_\eta = G - R\,, \tag{7}$$

$$\vec{j}_\eta = q_\eta \eta \mu_\eta \vec{E}_\eta - qD_\eta(\vec{\nabla}\eta)\,, \quad q_\eta = \begin{cases} e\,, & \eta = n \\ q\,, & \eta = p \end{cases}\,, \tag{8}$$

$$\vec{\nabla} \cdot (\varepsilon \vec{E}) = -q(n - p + N_a - N_d)\,, \tag{9}$$

$$\vec{j} = \vec{j}_n - \vec{j}_p\,, \tag{10}$$

$$\vec{E}_n = \vec{E} - \frac{1}{q}(\vec{\nabla} E_C)\,, \quad \vec{E}_p = \vec{E} - \frac{1}{q}(\vec{\nabla} E_V)\,. \tag{11}$$

The function G is the generation rate of carriers per unit volume, that is calculated by means of the OTSun program, discussed in Sec.2.1; R is the recombination rate of carriers per unit volume; N_a/N_d is the ionized acceptor/donor density; $E_C(E_V)$ is the edge energy of the conduction (valence) band; ε is the permittivity. Since the electric field strength $\vec{E} = -\vec{\nabla}\phi$ is related to the scalar potential ϕ, Eq.(9) transforms to the Poisson's equation.

We have extended the considered approach by adding the continuity equations for the energy density $\mathcal{E}_\eta = \eta \cdot \epsilon_\eta$ of electron-hole plasma

$$\frac{\partial \mathcal{E}_\eta}{\partial t} + \vec{\nabla} \cdot \vec{S}_\eta = -\mathcal{P}_\eta - \Gamma_\eta\,. \tag{12}$$

Here, $\mathcal{P}_\eta = \vec{j}_\eta \cdot \vec{E}_\eta$; $\Gamma_\eta = \eta(\epsilon_\eta - \epsilon_0)/\tau_{\epsilon_\eta}$, where τ_{ϵ_η} is the energy relaxation time, $\epsilon_0 = 3k_BT_0/2$. This extension is due to the fact that the mobility μ_η, and, correspondingly, the diffusion coefficient $D_\eta = \mu_\eta k_B T_0/q_\eta$ depend on

mean carrier energy ϵ_η. Here, k_B is the Boltzmann constant, T_0 is a solar cell temperature.

The energy flux density $\vec{S}_\eta$ has the following form

$$\vec{S}_\eta = \frac{1}{q}\gamma\epsilon_\eta\vec{j}_\eta - K_\eta(\vec{\nabla}\epsilon_\eta)\,, \tag{13}$$

where γ determines the differential thermo e.m.f. coefficient [see Ref.(36), p.430], K determines the thermal conductivity.

The rate of non-radiative, Shockley-Read-Hall (SRH), recombination has a standard form

$$R = (np - n_i^2)/(\tau_p n + \tau_n p)\,. \tag{14}$$

To study the efficiency of the solar cell we solve the set of Eqs.(7)-(14) only for the active layers of the solar cell structure (see Fig.1 and corresponding discussion in Sec.2.1).

The parameters for the contact and the perovskite layers have been taken from Refs.(37; 38), respectively. They are following for $TiO_2/CH_3NH_3PbI_3$/ Spiro-OMeTAD: the relative dielectric constant is 60/60/3; the effective electron mass is 1/1/1 ($\times m_e$); the effective hole mass is 1/1/1 ($\times m_e$); the electron mobility is 0.006/50/0.0001 ($\mathrm{cm}^2/(\mathrm{V}\cdot$ sec)); the hole mobility is 0.006/50/0.0001 ($\mathrm{cm}^2/(\mathrm{V}\cdot$ sec)); the carrier lifetime ($\tau_n = \tau_p = \tau$) is $10^{-9}/7.7\cdot 10^{-9}/10^{-9}$ (sec); the perovskite carrier lifetime value corresponds to the diffusion length of 1 μm. Here, m_e is a free electron mass.

In our calculations we use the following boundary conditions. In a heavily doped TiO_2 the majority carrier concentration is set to the value $n = N_d = 10^{19}(\mathrm{cm}^{-3})$, while the minority one is set to the value $p = n_i^2/N_d$. Here, n_i^2 is a carrier concentration in the intrinsic semiconductor [see for details Ref.(39)].

The opposite situation occurs over heavily doped Spiro-OMeTAD, where the majority carrier concentration is $p = N_a = 3\cdot 10^{18}(\mathrm{cm}^{-3})$, while the minority one is set to the value $n = n_i^2/N_a$. We assume that at boundaries (top and bottom boundaries of the active region in Fig.1) electron and hole subsystems have average energies as in thermal equilibrium $\epsilon_n = \epsilon_p = 3k_BT_0/2$.

When the p-i-n system is illuminated, light creates electron-hole pairs in the perovskite layer, while the contact layers have been considered to be transparent. In order to define the J–V characteristics of the considered system, one has to extract the contact potential difference from the applied voltage to the p-i-n structure by means of the standard procedure (39). At

a given voltage applied to the solar cell under the incident light, we are able to define the current over contacts. The numerical approach to the solution of the set of equations is discussed in details in (40).

2.4. Validation of the carrier transport model

To demonstrate the relevance of our model to experimental observations, we use the analogy of the PSC to a current generator in parallel with a diode. In addition, it is necessary to account for the parasitic resistance of the contacts and feeding conductors, R_S; the leakage resistance, related to the local short circuit of ETM/HTM layers, R_{sh}. Thus, we analyse the equivalent circuit, shown in Fig.3. Note, that a degree of the light reflection by the front surface (C_{refl}) may also affect the J–V characteristics of the real device (see Fig.1).

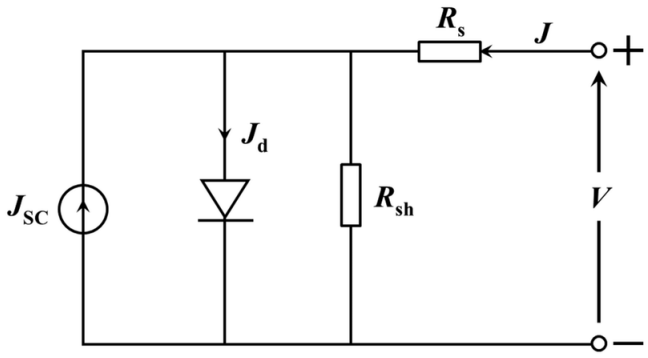

Figure 3: The circuit layout.

The J–V characteristics of the diode and the generator (Fig.3) can be evaluated with the aid of numerical solution of the transport equations (7-11). Such approach enables to us to establish the PCE dependence on the intrinsic solar cell properties such as the non-radiative recombination time of carries (τ); or, closely related to the latter, the diffusion length ($L_{dif} = \sqrt{D\tau}$).

We apply our model to simulate the J–V characteristics of several PSCs available in literature, considering the standard AM1.5 ASTM G-173-03 reference direct spectrum (34). All geometrical and electro-physical parameters of the real devices are taken from literature. On the other hand, to attain the best agreement between the measured and simulated J–V characteristics, we vary the following parameters: i) the diffusion length L_{dif}; ii) the parasitic

resistance R_S; iii) the leakage resistance R_{sh}; iv)the degree of light reflection C_{refl} (see Table 1).

$L_{dif}(\mu\text{m})$	R_S ($\Omega \times \text{cm}^2$)	R_{sh} ($\text{k}\Omega \times \text{cm}^2$)	C_{refl}	Ref
0.33	6.5	inf	0.19	(20)
1.85	5.2	inf	0.16	(41)
1.28	0	inf	0.09	(42)
8	3	0.09	0.07	(43)
9.4	4.5	1.8	0.0386	(44)
2.64	1.6	1.3	0.048	(45)
9.4	0.4	1.1	0	(46)

Table 1: The set of optimal values of the fitted variables.

The results of our analysis for available PSCs are summarized in Table 2. Note, that the calculations for the PCE, the fill factor (FF), the short circuit current (J_{sc}), and the open-circuit voltage (V_{oc}) are carried out under the assumption that all considered perovskite are undoped. It is important to emphasize that there is a good agreement between measured and simulated solar cell properties, based on our approach. This fact confirms, indeed, the validity and vitality of the carrier transport model, discussed Sec. 2.2.

PCE (%)		FF (%)		J_{sc}		V_{oc}		Ref
Exp	Sim	Exp	Sim	Exp	Sim	Exp	Sim	
11.4	11.6	64	64	20.3	20.2	0.89	0.89	(20)
15	14.5	73	73	20	20	0.993	0.995	(41)
15.7	15.6	74.9	74.4	20.4	20.4	1.03	1.03	(42)
17.91	18.32	73.6	75.7	21.84	21.77	1.114	1.112	(43)
19.3	19.3	75.01	75.17	22.75	22.69	1.13	1.13	(44)
19.71	19.92	76.2	77.4	23.83	23.80	1.086	1.082	(45)
22.1	22.3	80.3	80.5	25	25	1.1	1.1	(46)

Table 2: Comparison of the experimental and simulated results.

3. Discussion of results

3.1. Perovskite absorption

The experimental optimization of perovskite thin-films with the specular BSR suggests that the high efficiency devices possess the thickness of order

$400 \div 800$ nm (20). In order to find the optimal thickness in our calculations, we consider the following perovskite thickness: 50, 100 and 150 only for the Lambertian reflection; and 200, 300, 400, 500, 600, 800, 1000 nm for the specular and Lambertian reflections (see Fig.4). We recall that ray tracing simulations are carried out, emitting 1000 rays per each wavelength with a 2 nm step at the normal incidence.

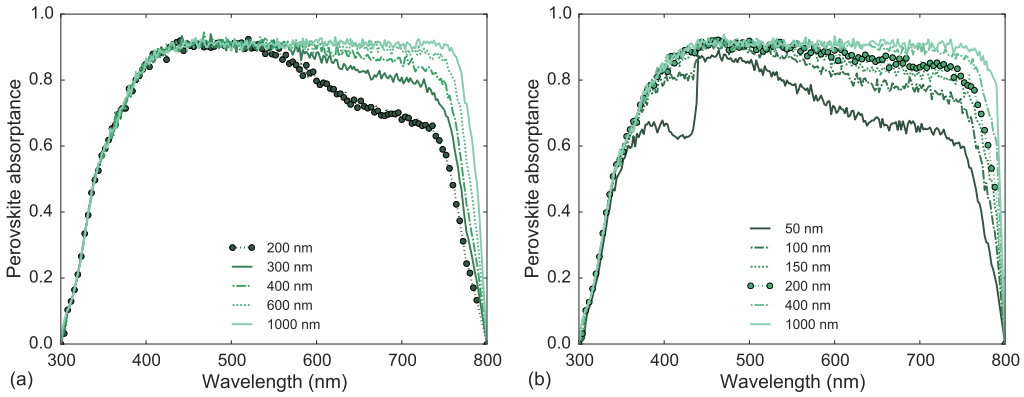

Figure 4: Perovskite absorptance spectra obtained by means of OTSun: (a) the specular reflection model; (b) the Lambertian reflection model.

The maximum of the absorptance is located in the wavelength interval $400 \div 550$nm in the case of the specular BSR (see Fig.4a). The increase of the perovskite layer thickness from 200 nm to higher values changes drastically the absorptance in the wavelength range of $500 \div 800$ nm. In contrast, in the case of the Lambertian reflection the absorptance has a notable change in the thickness interval $50 \div 200$ nm. While the maximum value is already reached for the small thickness for the wavelength range $400 \div 800$ nm, slowly improving with the thickness increase (see Fig.4b). Our calculations evidently demonstrate that perovskite layer of 400 nm (see Fig.4b) has almost the same absorptance as the one of the specular BSR case with the thickness of 1000 nm.

It is interesting to trace how many photons are absorbed with the increase of the perovskite layer thickness, with the specular and Lambertian BSR. We consider the standard AM1.5 ASTM G-173-03 reference direct spectrum (34). In this case the irradiance of 900W/m^2 is reaching the solar cell. Note, that the useful radiation is determined by the range of $300 \div 800$ nm. Hence, the useful irradiance is about 500 W/m^2. Taking these facts into account,

it follows that the number of emitted photons is 1.45×10^{21}. While the maximum of absorbed photons is 1.20×10^{21}. It appears that the Lambertian reflection leads to the larger number of absorbed photons at the smaller perovskite thickness (see Table 3). It is remarkable, that the perovskite layer of the thickness 200 nm, with the Lambertian scattering BSR, has almost the same number of the absorbed photons as the perosvkite layer of the thickness 500 nm with the specular BSR.

Perovskite thickness (nm)	% Absorbed photons	
	Specular Case	Lambertian Case
50	-	63.5%
100	-	72.7%
150	-	76.3%
200	68.7%	78.1%
300	74.4%	80.2%
400	77.3%	81.1%
500	78.9%	81.7%
600	79.7%	82.0%
800	80.7%	82.4%
1000	81.5%	82.6%

Table 3: The percentage of absorbed photons versus the perovskite thickness for the specular and Lambertian BSR.

The fraction of the energy absorbed by the non-photovoltaic materials is known as the parasitic losses. By integrating the absorptance over the wavelength, it is possible to compare the influence of parasitic losses with the perovskite absorption and the total reflectance, as a function of perovskite thickness (see Fig.5).

In the specular BSR case the amount of reflected energy increases with the thickness decrease, and reaches values slightly larger than 20% (see Fig.5a). In contrast, the parasitic losses decrease as the thickness decrease. On the other hand, the Lambertian BSR case (see Fig.5b) has lower values of reflectance, although the behavior is the same as in the latter case. In terms of the parasitic losses, they remain constant for the thicknesses greater than 200 nm, and increase when the thickness is lower, reaching up to 10%.

The ray tracing methodology allows to analyze the local behavior of the generation rate inside the perovskite (see Fig.6). In both cases (the specular and Lambertian reflection) the higher generation takes place for thinner

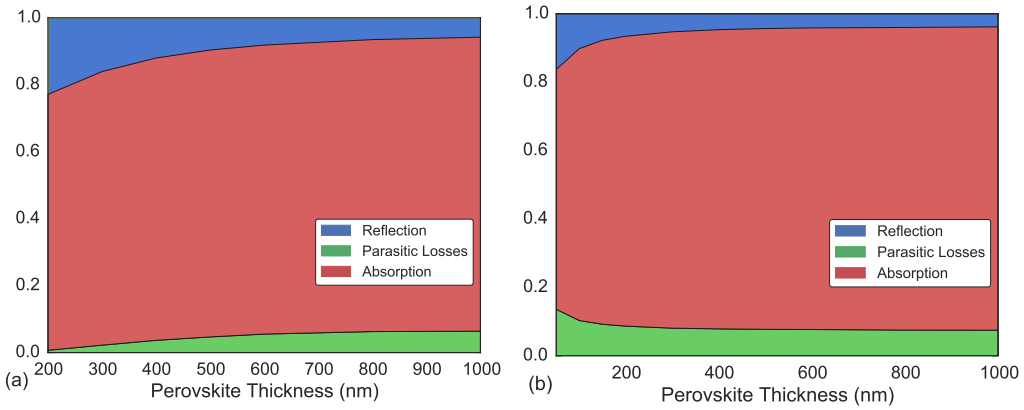

Figure 5: Parasitic losses, reflectance and absorptance in the PSC with specular (a) and Lambertian (b) BSR as a function of the perovskite layer thickness between 50 and 1000 nm. Calculated under the standard AM1.5 ASTM G-173-03 reference direct spectrum between a wavelength range of 300-800 nm.

perovskite layer. This is due to the fact that the smaller the thickness of the perovskite, the greater the density of absorbed photons and, therefore, the value of the generation, as discussed bellow.

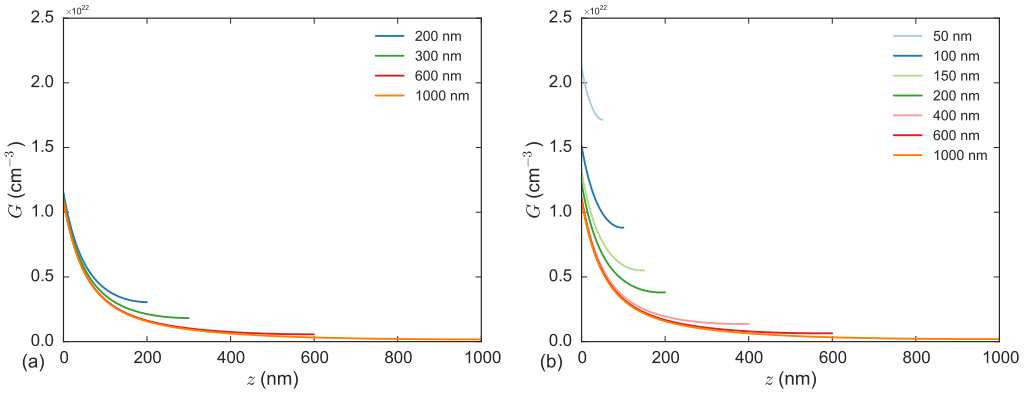

Figure 6: Generation rate obtained by means of OTSun: (a) the specular reflection model; (b) the Lambertian reflection model.

We name the "forward generation" the one, that is produced due to the ray absorption in forward direction, without any internal reflection. This generation decreases with the increase of the thickness of the perovskite sample [see cases (a) and (b) in Fig.7)]. On the other hand, we name the genera-

tion, produced by any internal reflection, as the "light trapping generation". In the case of the Lambertian scattering BSR the light trapping generation remains almost constant, independently on the perovskite thickness.

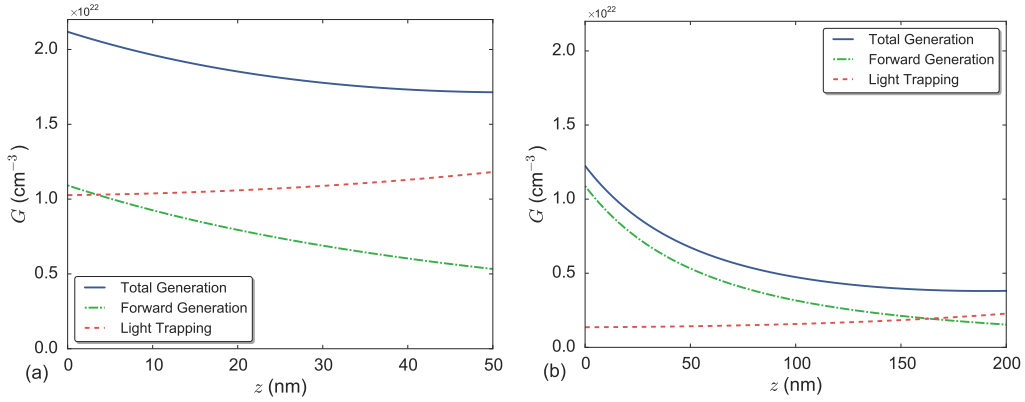

Figure 7: Total generation rate (solid blue line), the light trapping generation (dashed red line) and the forward generation (dashed-dot green line). The results are presented for the perovskite thickness:(a) 50 nm; (b) 200 nm.

3.2. Efficiency

The light trapping yields a sensible change, improving the absorption of the thin layer. As a result, it becomes comparable with the absorption of the thicker one (see Table 2 and Fig.4). Indeed, due to the improved absorption, the J–V characteristics with the Lambertian reflection own more efficiency in contrast to those of the specular case for thin films (compare the J–V characteristics for the thickness $\sim 200, 300$ nm in Fig.8). However, with the increase of the thickness the difference between two cases becomes negligible (compare the J–V characteristics for the thickness 1000 nm). In this connection, although the thick PSC insures the absorption of all photons with the energy larger than a semiconductor band gap, it also introduces additional energy losses that set a trade-off relationship between the efficiency and the thickness (35).

Before to discuss the optimal conditions for the efficiency, there are a few comments in order. Two well-known effects are expected in thin solar cells. The first one is the reduction of the short-circuit current of the solar cell ($J_{\rm sc}$), since the thinner semiconductor film the lesser light is absorbed by the film. The second one is the increase of the open circuit voltage $V_{\rm oc}$. In

particular, this effect is attributed to the dependence of the forward diode current (governed by the recombination) on the device thickness (13). These two effects affect the PCE ($\eta \sim J_{\rm sc}V_{\rm oc}$) in opposite directions. Evidently, their interplay should be essential for the optimal thickness of PSCs.

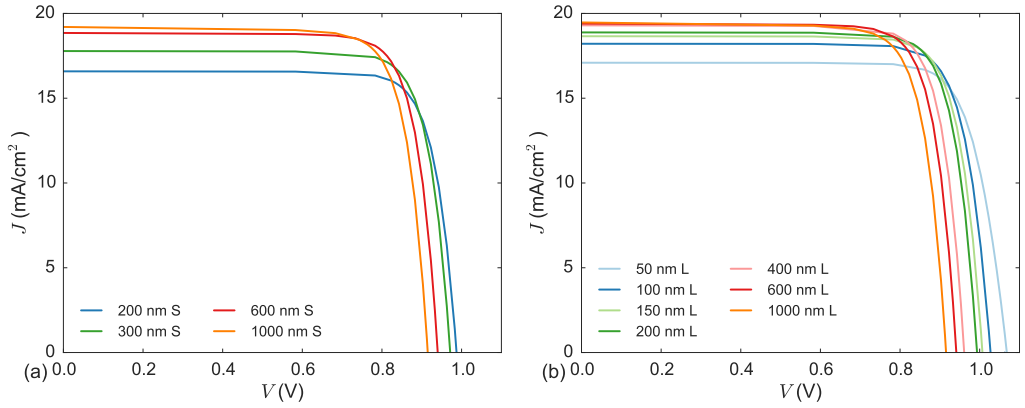

Figure 8: J–V characteristics of the PSC as a function of the perovskite layer thickness: (a) the specular reflection; (b) the Lambertian scattering.

To gain a better insight into this phenomenon let us consider the mechanisms that determine J–V characteristics. We recall that the current of an illuminated PSC is the difference between the dark current $J_{\rm dark}$ that depends on the terminal voltage; and the constant photocurrent $J_{\rm ph}$, that flows in the opposite direction (39). It is well known that the thicker the absorber layer, the larger the recombination; and, consequently, the larger the dark current.

In order to simplify discussion, let us consider an ideal p-n diode. In the limit the layer thickness $d \ll L_{dif}$ (13), the dark current (for example, in the n-doped semiconductor) can be written in the form

$$J_{\rm dark} = q\frac{n_{\rm av}d}{\tau}\,, \quad n_{\rm av} = n_p(\exp^{\frac{qV}{k_BT}} - 1)\,, \tag{15}$$

where n_p is the density of the minority carrier concentration. We have assumed that $\tau_n = \tau_p = \tau$. At open circuit conditions there is the equality between the dark current and the short circuit photocurrent: $J_{\rm sc} \equiv J_{\rm ph} \rightarrow J_{\rm ph} - J_{\rm dark} = 0$. We recall that the dark current is also equivalent to the recombination current. At the conditions: i) $n_p = const$, ii) $\tau = const$, the decrease of the thickness d [see Eq.(15)] requires the increase of $V_{\rm oc}$ due to

the condition iii) $J_{\rm dark} = J_{\rm ph}$. Thus, it follows that the open circuit voltage $V_{\rm oc}$ increases with the decreasing of the thickness d.

In the p-i-n diode, however, the recombination takes place in the i-region. To illuminate this fact in the case under investigation, we analyse the band profile of the PSC p-i-n structure with chosen parameters (see Fig.9). The barrier at the conduction band blocks electron motion, while the barrier at valence band blocks hole motion at forward diode bias. Evidently, the forward current value is defined by the total number of recombined electrons and holes injected in perovskite.

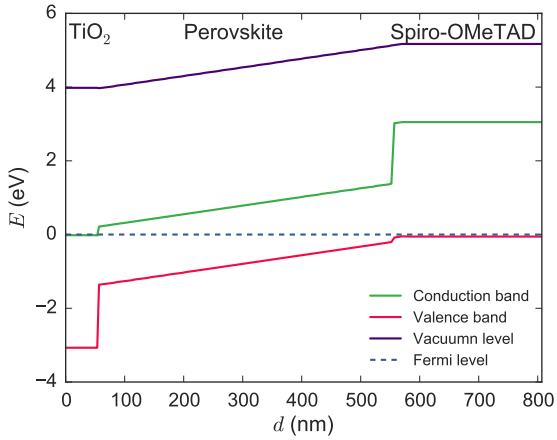

Figure 9: Band diagram of the PSC with the perovskite layer of the thickness 500 nm.

The standard models [e.g., (47)] are based on the approximation of the constant electric field. This approximation is well justified at zero applied voltage. It becomes poor, however, when the applied voltage approaches the built-in voltage value. In this case we are faced with the nonconstant electric field, especially, in the vicinity of the blocking contacts [see Fig.10(a)].

Nevertheless, we can use the above discussion to shed light in this case. The results of our calculations demonstrate evidently [see Fig.10(b)] that the contribution of the contact regions is negligible in the recombination process. The forward current value is defined by the total number of recombined electrons and holes injected in the perovskite.

Without loss of generality, let us consider the one-dimensional case. Due to potential barriers the current is determined, basically, by the recombination of carriers inside the perovskite absorber. At $\tau_n = \tau_p = \tau$, in the steady

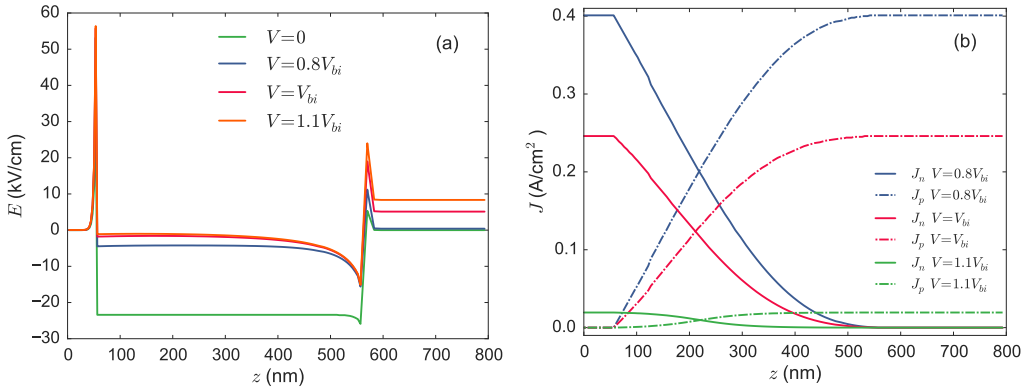

Figure 10: (a) Simulated electric field in the n-i-p PSC with d=500 nm in the dark at different applied voltages. At V= 0 electric field is created by the built-in potential ($V_{\rm bi} = 1.18$V for the structure simulated). (b) Simulated electron J_n and J_p dark current variation along the total current path $J = J_n(x) + J_p(x) = const$ in the n-i-p PSC with d=500 nm in the dark at different applied voltages.

regime ($\partial\eta/\partial t = 0$) for the dark current ($G = 0$), we have (see Eq.7)

$$\frac{\partial J}{\partial x} = -qR \Rightarrow J_{\rm dark} = J_{\rm rec} = J_n(0) = J_p(W) = q\frac{n_{\rm av}d}{\tau}\,, \qquad (16)$$

$$n_{\rm av} = \frac{1}{W}\int_0^W \frac{np - n_i^2}{n+p}dx\,, \qquad (17)$$

where the thickness $W = d + d_{\rm TiO_2} + d_{\rm Spiro-OMeTAD}$.

For the p-i-n structure our simulations demonstrate a weak dependence of the $n_{\rm av}$ with the increase of the thickness, while the recombination current $J_{\rm rec}$ increases almost linear with the thickness increase (see Fig.11). Hence, we conclude that the increase of the open circuit voltage $V_{\rm oc}$ with the decrease of the absorber thickness is due to the decrease of the recombination in thinner diodes. It is the reminiscence of the phenomenon that takes place in the p-n junction. However, the recombination in the p-i-n system decreases faster with the decrease of the absorber thickness.

Now we are ready to discuss the impact of the light trapping mechanism on the PCE of the PSC. In accordance with the above discussion, the result of calculations demonstrates the decrease of $V_{\rm oc}$ with the increase of the PSC thickness, for the Lambertian and specular reflections [see Fig.12(a)]. In contrast, the increase of the thickness yields the increase of the short circuit current $J_{\rm sc}$ [see Fig.12(b)]. Note, the presence of the Lambertian BSR is the

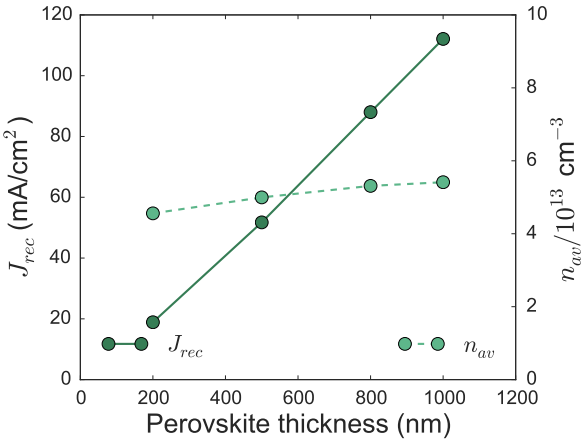

Figure 11: Recombination current decreases with the perovskite thickness in equally biased not illuminated n-i-p PSCs.

determining factor of the enhanced corresponding current in thin samples $200 \leq d \leq 1000$ nm. It appears that with further increase of the thickness the current tends to an asymptotic limit, independent on the nature of the BSR. In other words, the increased absorption in the PSC with the Lambertian BSR due to the thickness does not affect J_{sc} that changes only slightly with the thickness.

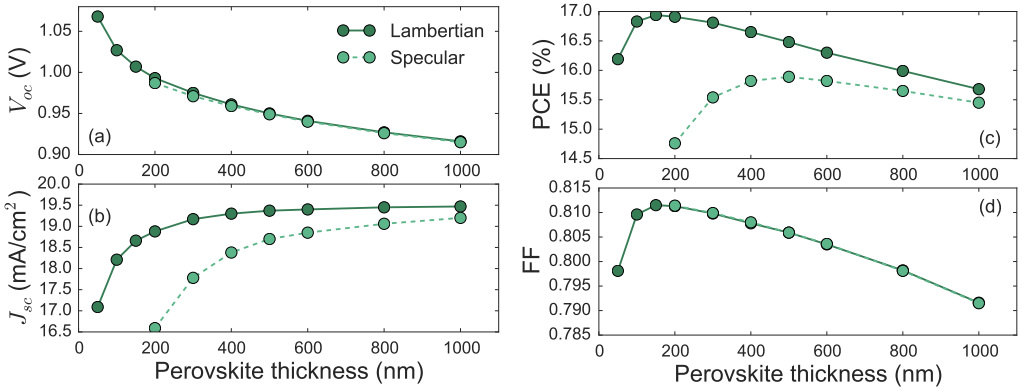

Figure 12: The open circuit voltage (a), the short circuit photocurrent density (b), the power conversion efficiency (c), and the fill factor (d) as a function of the perovskite thickness.

The behaviour of the J–V characteristics (V_{oc} and J_{sc}) with the increase of

d leads to the PCE maximum for the specular BSR around $d \simeq 500$ nm [see Fig.12(c)]. In contrast, in the PSC with the Lambertian BSR the thickness decrease leads to the increase of the open circuit voltage $V_{\rm oc}$ [see Fig.12(a)] and to a minor decrease of the open circuit current $J_{\rm sc}$ [see Fig.12(b)]. As a result, the thickness decrease in this PSC leads to a monotonic increase of the device effectiveness up to the optimal thickness ~ 150 nm [see Fig.12(c)]. The further decrease of the thickness decreases the PCE. However, this conclusion should be taken with a caution, since there are effects not taken into account in our consideration (i.e., possible structural defects due to small thickness etc). Note, that the FF being less sensitive to the thickness is almost the same in the both considered cases [see Fig.12(d)].

The PSC efficiency with the Lambertian BSR yields the figure 17% for thin absorbers (~ 150 nm) in comparison with the one with the specular reflection with 14.7% of the PCE. In fact, for this thin PSC the PCE ($\simeq 17\%$) is even larger than the maximal one ($\simeq 15.8\%$) of the relatively thick solar cell (~ 500 nm) with the specular BSR. Indeed, we find that there are a few factors responsible for this increase of the PCE. The use of wide band gap contacts (electron/hole transport materials) leads to a steep decrease of the device forward dark current with the decrease of the PSC thickness. Consequently, there is a fast increase of the open circuit voltage. Another factor is the decrease of the recombination with the decrease of the thickness. Thus, the advantage of the light trapping is twofold: i) it allows to decrease the PSC thickness in order to attain the efficiency optimum; ii) it increases the maximum device efficiency.

It is important to stress that the PCE of the perovskite solar cell could be increased noticeably with the increase of the diffusion length of the perovskite layer (see Fig.13). Note, that the diffusion length is much larger than the perovskite thickness in the considered case. As a result, all photogenerated carriers can reach the corresponding contacts. In fact, by the increase of the diffusion length we increase the carrier life-time. Consequently, we decrease further the dark current [see Eq.(16)], i.e., increase the PCE of the perovskite solar cell.

4. Conclusions

In this paper we investigate the role of BSR on the efficiency of a typical perovskite thin-film solar cell (see Fig.1). In order to describe the optical performance of this cell we carry out the analysis using both the ray tracing

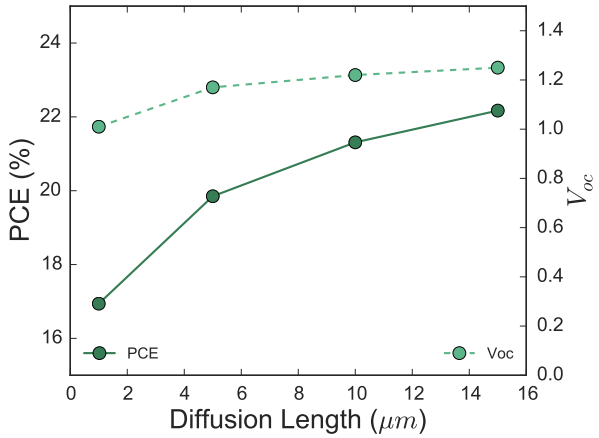

Figure 13: The PCE and V_{oc} as a function of the diffusion length L_{dif}. The perovskite thickness is $d = 150$ nm; the Lambertian scattering is considered in the BSR.

simulations and the transfer-matrix method. To perform the ray tracing simulations, OTSun python package has been used.

We found that the Lambertian scattering increases the absorptance essentially for the wavelength $500 \leq \lambda \leq 800$ nm in the cell with the thickness $\sim 200 \div 600$ nm. The use of the Lambertian BSR allows to obtain the same absorption at twice thinner cell in comparison with the specular BSR (see Table 1). From our results it follows that the cell with the thickness 200 nm with the Lambertian BSR demonstrates an absorptance of 78.1%, surpassing the 77.3% of the 400 nm with the specular BSR.

To calculate the J–V characteristics of the solar cell we have employed the model for the carrier transport (35). By means of this model and the calculated absorptance we have obtained that the high power efficiency can be achieved for the solar cell with the thickness of order $\sim$ 150 nm with the Lambertian reflection. We have found that the maximal PCE can be achieved in the thin film perovskite solar cell due to the decrease of the recombination current. If the open circuit voltage would be similar with respect to the PSC thickness at the specular and Lambertian reflection, one could obtain the same PCE in PSCs with nearly equal optical paths: in a thin PSC with the light trapping mechanism and in a thick PSC with the specular reflection. However, we have found that the thin PSC with the light trapping mechanism has the higher PCE value always. It is due to the decrease of the recombination leakage and the increase of the open circuit

voltage with the decrease of the PSC thickness.

5. Acknowledgements.

This work is partially supported by the Spanish Ministry of Economy and Competitiveness (MINECO) and the European Regional Development Funds (ERDF) [ENE2015-68339-R]. It has also been co-funded by the Vicepresidency and Innovation, Research and Tourism Department of the Government of the Balearic Islands and the European Social Fund (ESF).

6. References.

[1] T. D. Lee, A. U. Ebong, A review of thin film solar cell technologies and challenges, Renewable and Sustainable Energy Reviews-doi:10.1016/j.rser.2016.12.028.

[2] S. Demic, A. N. Ozcivan, M. Can, C. Ozbek, M. Karakaya, Recent Progresses in Perovskite Solar Cells, InTech, 2017. doi:10.5772/65019.
URL http://www.intechopen.com/books/nanostructured-solar-cells/recent-progresses-in-perovskite-solar-cells

[3] M. A. Green, Y. Hishikawa, E. D. Dunlop, D. H. Levi, J. Hohl-Ebinger, M. Yoshita, A. W. Ho-Baillie, Solar cell efficiency tables (Version 53), Progress in Photovoltaics: Research and Applications 27 (1) (2019) 3–12. doi:10.1002/pip.3102.
URL http://doi.wiley.com/10.1002/pip.3102

[4] J. Bos-Coenraad, L. Bunthof, J. Schermer, Scientrace: An open source, programmable 3D ray tracer, Solar Energy 155 (2017) 1188–1196. doi:10.1016/J.SOLENER.2017.07.003.
URL https://www.sciencedirect.com/science/article/pii/S0038092X17305777?via{\%}3Dihub

[5] T. Yagi, Y. Uraoka, T. Fuyuki, Ray-trace simulation of light trapping in silicon solar cell with texture structures, Solar Energy Materials and Solar Cells 90 (16) (2006) 2647–2656. doi:10.1016/j.solmat.2006.02.031.

[6] V. Magnin, J. Harari, M. Halbwax, S. Bastide, D. Cherfi, J. P. Vilcot, Angle-dependent ray tracing simulations of reflections on pyramidal textures for silicon solar cells, Solar Energy 110 (2014) 378–385.

doi:10.1016/j.solener.2014.09.025.
URL http://dx.doi.org/10.1016/j.solener.2014.09.025

[7] S.-J. Byun, S. Yong Byun, J. Lee, J. Wan Kim, T. Sung Lee, W. Mok Kim, Y. Kyu Park, K. Cho, An optical simulation algorithm based on ray tracing technique for light absorption in thin film solar cells, Solar Energy Materials and Solar Cells 95 (1) (2011) 408–411. doi:10.1016/j.solmat.2010.04.017.
URL http://dx.doi.org/10.1016/j.solmat.2010.04.017

[8] N. Tucher, J. Eisenlohr, H. Gebrewold, P. Kiefel, O. Höhn, H. Hauser, J. C. Goldschmidt, B. Bläsi, Optical simulation of photovoltaic modules with multiple textured interfaces using the matrix-based formalism OPTOS, Optics Express 24 (14) (2016) A1083. doi:10.1364/OE.24.0A1083.
URL https://www.osapublishing.org/abstract.cfm?URI=oe-24-14-A1083

[9] J. M. Ball, S. D. Stranks, M. T. Hörantner, S. Hüttner, W. Zhang, E. J. W. Crossland, I. Ramirez, M. Riede, M. B. Johnston, R. H. Friend, H. J. Snaith, Optical properties and limiting photocurrent of thin-film perovskite solar cells, Energy & Environmental Science 8 (2) (2015) 602–609. doi:10.1039/C4EE03224A.
URL http://xlink.rsc.org/?DOI=C4EE03224A

[10] S. M. Iftiquar, J. Yi, Numerical simulation and light trapping in perovskite solar cell, Journal of Photonics for Energy 6 (2) (2016) 025507. doi:10.1117/1.JPE.6.025507.
URL http://photonicsforenergy.spiedigitallibrary.org/article.aspx?doi=10.1117/1.JPE.6.025507

[11] A. Peer, R. Biswas, J.-M. Park, R. Shinar, J. Shinar, Light management in perovskite solar cells and organic LEDs with microlens arrays, Optics Express 25 (9) (2017) 10704. doi:10.1364/OE.25.010704.
URL https://www.osapublishing.org/abstract.cfm?URI=oe-25-9-10704

[12] K. Jäger, L. Korte, B. Rech, S. Albrecht, Numerical optical optimization of monolithic planar perovskite-silicon tandem solar cells with regular and inverted device architectures, Optics Express 25 (12) (2017) A473. doi:10.1364/OE.25.00A473.

URL https://www.osapublishing.org/abstract.cfm?URI=oe-25-12-A473

[13] A. A. Luque, S. Hegedus, Handbook of photovoltaic science and engineering, Wiley, 2011.

[14] G. Cardona, R. Pujol-Nadal, OTSun Python Package, https://github.com/bielcardona/OTSun (2018).
URL https://github.com/bielcardona/OTSun

[15] FreeCAD: Your Own 3D Parametric Modeler.
URL https://www.freecadweb.org/

[16] OTSunWebApp.
URL http://otsun.uib.es/otsunwebapp/node/start

[17] F. Bonnn-Ripoll, G. Cardona, R. Nadal-Pujol, Tutorial 2 OTSun Web App.
URL https://github.com/bielcardona/OTSun/blob/master/OTSunWebApp/Tutorial_2_1e_OTSun_WebApp.pdf

[18] H. A. Macleod, Thin-film optical filters, CRC Press/Taylor & Francis, 2010.

[19] H. J. Snaith, Perovskites: The emergence of a new era for low-cost, high-efficiency solar cells, Journal of Physical Chemistry Letters 4 (21) (2013) 3623–3630. arXiv:nn504795v, doi:10.1021/jz4020162.

[20] G. E. Eperon, V. M. Burlakov, P. Docampo, A. Goriely, H. J. Snaith, Morphological control for high performance, solution-processed planar heterojunction perovskite solar cells, Advanced Functional Materials 24 (1) (2014) 151–157. doi:10.1002/adfm.201302090.

[21] P. M. Kaminski, P. J. Isherwood, G. Womack, J. M. Walls, Optical Optimization of Perovskite Solar Cell Structure for Maximum Current Collection, Energy Procedia 102 (May) (2016) 11–18. doi:10.1016/j.egypro.2016.11.312.
URL http://dx.doi.org/10.1016/j.egypro.2016.11.312

[22] S. D. Stranks, G. E. Eperon, G. Grancini, C. Menelaou, M. J. P. Alcocer, T. Leijtens, L. M. Herz, A. Petrozza, H. J. Snaith, Electron-Hole Diffusion Lengths Exceeding Trihalide Perovskite Absorber, Science 342 (October) (2013) 341–344. arXiv:0404368, doi:10.1126/science.1243982.

[23] L. K. Ono, M. R. Leyden, S. Wang, Y. Qi, Organometal halide perovskite thin films and solar cells by vapor deposition, J. Mater. Chem. A 4 (18) (2016) 6693–6713. doi:10.1039/C5TA08963H.
URL http://xlink.rsc.org/?DOI=C5TA08963H

[24] H. Zhou, Q. Chen, G. Li, S. Luo, T. B. Song, H. S. Duan, Z. Hong, J. You, Y. Liu, Y. Yang, Interface engineering of highly efficient perovskite solar cells, Science 345 (6196) (2014) 542–546. doi:10.1126/science.1254050.

[25] P. Löper, M. Stuckelberger, B. Niesen, J. Werner, M. Filipič, S.-J. Moon, J.-H. Yum, M. Topič, S. De Wolf, C. Ballif, Complex Refractive Index Spectra of CH3NH3PbI3 Perovskite Thin Films Determined by Spectroscopic Ellipsometry and Spectrophotometry, The Journal of Physical Chemistry Letters 6 (1) (2015) 66–71. doi:10.1021/jz502471h.
URL http://pubs.acs.org/doi/10.1021/jz502471h

[26] M. J. Dodge, Refractive properties of magnesium fluoride, Applied Optics 23 (12) (1984) 1980. doi:10.1364/AO.23.001980.
URL https://www.osapublishing.org/abstract.cfm?URI=ao-23-12-1980

[27] T. Siefke, S. Kroker, K. Pfeiffer, O. Puffky, K. Dietrich, D. Franta, I. Ohlídal, A. Szeghalmi, E.-B. Kley, A. Tünnermann, Materials Pushing the Application Limits of Wire Grid Polarizers further into the Deep Ultraviolet Spectral Range, Advanced Optical Materials 4 (11) (2016) 1780–1786. doi:10.1002/adom.201600250.
URL http://doi.wiley.com/10.1002/adom.201600250

[28] C.-W. Chen, S.-Y. Hsiao, C.-Y. Chen, H.-W. Kang, Z.-Y. Huang, H.-W. Lin, Optical properties of organometal halide perovskite thin films and general device structure design rules for perovskite single and tandem solar cells, Journal of Materials Chemistry A 3 (17) (2015) 9152–9159. doi:10.1039/C4TA05237D.
URL http://xlink.rsc.org/?DOI=C4TA05237D

[29] Optical Data from Sopra SA (2008).
URL http://www.sspectra.com/sopra.html

[30] Schott, Optical Glass, Stress: The International Journal on the Biology of Stress.
URL https://refractiveindex.info/?shelf=glass&book=BK7&page=SCHOTT

[31] H. U. Yang, J. D'Archangel, M. L. Sundheimer, E. Tucker, G. D. Boreman, M. B. Raschke, Optical dielectric function of silver, Physical Review B 91 (23) (2015) 235137. doi:10.1103/PhysRevB.91.235137.
URL https://link.aps.org/doi/10.1103/PhysRevB.91.235137

[32] Refractive Index Database Table of Refractive Index Values for Thin Film Thickness Measurement.
URL https://www.filmetrics.com/refractive-index-database

[33] Steven Byrnes, tmm 0.1.7 : Python Package Index, https://pypi.python.org/pypi/tmm (2017).
URL https://pypi.python.org/pypi/tmm

[34] Solar Spectral Irradiance: ASTM G-173 (2012).
URL http://rredc.nrel.gov/solar/spectra/am1.5/astmg173/astmg173.html

[35] Y. B. Martynov, R. G. Nazmitdinov, A. Moià-Pol, P. P. Gladyshev, A. R. Tameev, A. V. Vannikov, M. Pudlak, On the efficiency limit of $ZnO/CH_3NH_3PbI_3/CuI$ perovskite solar cells, Phys. Chem. Chem. Phys. 19 (30) (2017) 19916–19921. doi:10.1039/C7CP03892E.
URL http://xlink.rsc.org/?DOI=C7CP03892E

[36] S. G. Kalashnikov, V. L. Bonch-Bruevich, The Physics of Semiconductors (Russian Edition), Moscow: Main Editorial Board for Physical and Mathematical Literature, 1990.

[37] O. O. Madelung, Semiconductors : Data Handbook, Springer Berlin Heidelberg, 2004.

[38] M. A. Green, A. Ho-Baillie, H. J. Snaith, The emergence of perovskite solar cells, Nature Photonics 8 (7) (2014) 506–514.

doi:10.1038/nphoton.2014.134.
URL http://dx.doi.org/10.1038/nphoton.2014.134

[39] S. M. Sze, K. K. Ng, Physics of semiconductor devices, Wiley-Interscience, 2007.

[40] Y. B. Martynov, A special form of boundary conditions for a the set of equations of low-temperature plasma, Zh. Vychisl. Mat. Mat. Fiz 39 (2) (1999) 309–314.
URL http://www.mathnet.ru/eng/agreement

[41] J. Burschka, N. Pellet, S.-J. Moon, R. Humphry-Baker, P. Gao, M. K. Nazeeruddin, M. Grätzel, Sequential deposition as a route to high-performance perovskite-sensitized solar cells, Nature 499 (7458) (2013) 316–319. doi:10.1038/nature12340.
URL http://www.nature.com/articles/nature12340

[42] D. Liu, T. L. Kelly, Perovskite solar cells with a planar heterojunction structure prepared using room-temperature solution processing techniques, Nature Photonics 8 (2) (2014) 133–138. doi:10.1038/nphoton.2013.342.
URL http://www.nature.com/articles/nphoton.2013.342

[43] N. J. Jeon, J. H. Noh, W. S. Yang, Y. C. Kim, S. Ryu, J. Seo, S. I. Seok, Compositional engineering of perovskite materials for high-performance solar cells, Nature 517 (7535) (2015) 476–480. doi:10.1038/nature14133.
URL http://www.nature.com/articles/nature14133

[44] Y. Zhou, C. Fuentes-Hernandez, J. Shim, J. Meyer, A. J. Giordano, H. Li, P. Winget, T. Papadopoulos, H. Cheun, J. Kim, M. Fenoll, A. Dindar, W. Haske, E. Najafabadi, T. M. Khan, H. Sojoudi, S. Barlow, S. Graham, J.-L. Brédas, S. R. Marder, A. Kahn, B. Kippelen, A universal method to produce low-work function electrodes for organic electronics., Science (New York, N.Y.) 336 (6079) (2012) 327–32. doi:10.1126/science.1218829.
URL http://www.ncbi.nlm.nih.gov/pubmed/22517855

[45] N. Ahn, D.-Y. Son, I.-H. Jang, S. M. Kang, M. Choi, N.-G. Park, Highly Reproducible Perovskite Solar Cells with Average Efficiency of 18.3% and Best Efficiency of 19.7% Fabricated via Lewis Base Adduct

of Lead(II) Iodide, Journal of the American Chemical Society 137 (27) (2015) 8696–8699. doi:10.1021/jacs.5b04930.
URL http://pubs.acs.org/doi/10.1021/jacs.5b04930

[46] W. S. Yang, B.-W. Park, E. H. Jung, N. J. Jeon, Y. C. Kim, D. U. Lee, S. S. Shin, J. Seo, E. K. Kim, J. H. Noh, S. I. Seok, Iodide management in formamidinium-lead-halide-based perovskite layers for efficient solar cells., Science (New York, N.Y.) 356 (6345) (2017) 1376–1379. doi:10.1126/science.aan2301.
URL http://www.ncbi.nlm.nih.gov/pubmed/28663498

[47] R. S. Crandall, Modeling of thin film solar cells: Uniform field approximation, Journal of Applied Physics 54 (12) (1983) 7176–7186. doi:10.1063/1.331955.
URL http://aip.scitation.org/doi/10.1063/1.331955